Dynamic Channel Modeling at 2.4 GHz for On-Body Area Networks

Lingfeng Liu, Raffaele D'Errico, Laurent Ouvry, Philippe De Doncker, and Claude Oestges

***Abstract*—In wireless body area networks, on-body radio propagation channels are typically time-varying, because of the frequent body movements. The dynamic local body scattering dominates the temporal and spatial properties of the on-body channels. The influence varies largely depending on the distribution of the channels and the modes of body movements. In this paper, we present some major achievements on the dynamic on-body channel modeling at 2.4 GHz under the framework of the COST 2100 action. Results of two complementary measurement campaigns are presented: a geometry-based one on a single subject, and a scenario-based one covering different subjects. Statistical models including the Doppler spectrum and the spatial correlation of on-body channels are presented. An analytical model is also introduced to offer a time-space description of the on-body channels, which is validated by the geometry-based measurement campaign.**

***Index Terms*—Body area networks, on-body channel, time-variant channel fading, body shadowing, channel spatial correlation, dynamic body scattering**

I. Introduction

WIRELESS body area networks (WBANs) have recently received a growing interest in scientific and industrial communities by the promising prospects across a range of applications, including remote medical services, sport monitoring, personal entertainments, etc.. WBANs are featured as low-power, low data rate, and person-centric wireless communications. They are usually composed of compact computing units working in a close range of the human body. WBANs are typically suitable for medical monitoring and other bio-telemetry applications, i.e. using body-worn sensors to collect and convey important bio-signals. The strict requirements on the power consumption and long-term transmission stability raise many challenges to WBANs on e.g. the antenna design and the channel characterization. The design of WBAN systems includes different frequencies, like the ISM bands at 400 MHz, 900 MHz, and 2.4 GHz [1]–[3], and the ultra-wide band (UWB) [4]. Moreover, the use of existing short-range communication standards, like Bluetooth and Zigbee/IEEE 802.15.4 at 2.4 GHz, provide a low-cost WBAN solution, has also attracted many studies [5].

L. Liu is with ICTEAM Electrical Engineering, Université catholique de Louvain, BELGIUM, and OPERA, Université libre de Bruxelles, BELGIUM. email: lingfeng.liu@uclouvain.be

R. D'Errico and L. Ouvry are with CEA, LETI, MINATEC 17 rue des Martyrs 38054 Grenoble Cedex 9, FRANCE. emails: raffaele.derrico@cea.fr, laurent.ouvry@cea.fr

P. De Doncker is with OPERA, Université libre de Bruxelles, BELGIUM. email: pdedonck@ulb.ac.be

C. Oestges is with ICTEAM Electrical Engineering, Université catholique de Louvain, BELGIUM. email: claude.oestges@uclouvain.be

Manuscript submitted May 30, 2011; revised July 18, 2011

The on-body propagation, i.e. radio waves propagating on the body surface, is a fundamental transmission mechanism in WBANs, either in the collecting and relaying of signals from the body-worn sensors to body-worn data sinks, or in peer-to-peer communications between the sensors. Unlike large-scale propagation, on-body propagation are dominated by the local body scattering, which not only forms a high path loss in a short distance on the body surface [3], [4], but also forms a time-variation (fading) of the on-body channels due to the body movements [2], [3]. The time-variation is an inevitable property of on-body channels because our bodies always move in realistic applications. The difficulty to understand the local body scattering is that the interaction among the transmitter (Tx), receiver (Rx), and the body occurs in a few wavelengths, which will complicate the scattering process and generates different influences to the on-body channels depending on the channel distribution, the polarization, and the body posture, not to mention the modified antenna gain when placed close to the skin. Consequently, the channel characteristics, e.g. on the fading variance and the Doppler dispersion, should reflect the effects of body scattering consistently.

Although complex simulations like finite-difference time-domain (FDTD) can give a precise and high-solution field description of static on-body propagation as in [6], extending such simulations into dynamic cases is usually too costly that most of the studies stay on statistical approaches or simplified analytical models. The dynamic on-body channels have also been partly addressed by the IEEE 802.15.6 standardization group [7]. However, the final channel model for on-body applications in [8], is mainly focused on static scenarios. Other studies like [9], [10], were limited by their test-beds and the understanding of the on-body propagation mechanisms, which exclude some critical aspects of the dynamic on-body channels, like the Doppler spectrum and the space-time fading correlation.

The WBAN channel modeling activities under the framework of the Special Interest Group E (SIG-E) of the COST 2100 action [11] have been focusing on different aspects of the dynamic on-body channels. The researches not only cover those featured in IEEE 802.15.6, but also try to fulfill the needs for the design of cooperative protocols. In this paper, we present an overview of the achieved results on dynamic on-body channel characterization and modeling by UCL-ULB and CEA-LETI in the COST 2100 action. Two independent measurement campaigns are presented. The complementary results from the measurements provide a complete statistical survey of the dynamic on-body channels at 2.4 GHz, including a geometry-based investigation on a single subject in UCL-

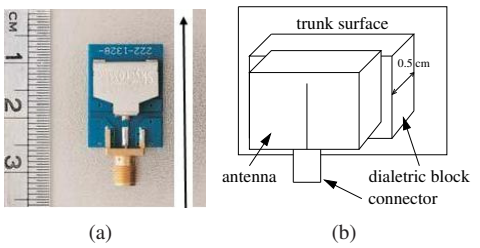

(a) (b)

Fig. 1. Antennas in measurement setup 1, (a) shows the antenna structure where the arrow indicates the antenna polarization, (b) describes the antenna emplacement on the trunk surface

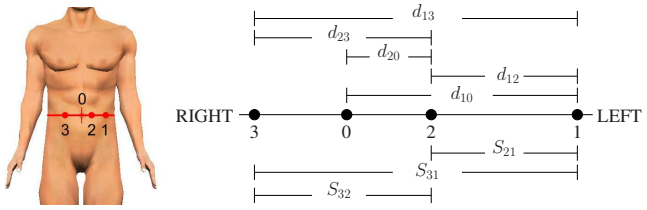

(a) (b)

Fig. 2. Measurement setup 1: (a) measured channels where 1, 2, 3 represent the antennas and 0 represents the trunk center; (b) geometric quantization of the scenarios, where S_{xy} with $x, y = 1, 2, 3$, represents the investigated channel with Tx, y, and Rx, x, d_{y0} is the transmitter absolute position, and d_{xy} is the propagation distance on the trunk surface.

ULB, and a scenario-based one on multiple subjects in CEA-LETI. An analytical model is also introduced to provide a physical time-space description of the on-body channels with respect of small-scale body movements.

The paper is organized as follows, Sec. II describes the context of the two measurement campaigns, Sec. III to Sec. V present the statistical characterization and modeling of the time-varying channel fading, Sec. VI introduces the analytical model, and Sec. VII offers some conclusive comments on the present work.

II. Measurements context

In this section, we present the contexts of two on-body channel measurement campaigns carried out at UCL-ULB and CEA-LETI respectively. The two measurement campaigns differ in terms of the test-beds, the scenarios, and the analyzing methods. Still, the collected results enable complementary approaches in on-body channel characterization.

A. Measurement setup 1

The measurement campaign from UCL-ULB was carried out in a quasi-anechoic environment. Three linearly polarized antennas (Skycross SMT-3TO10M), as depicted in Fig. 1(a), were attached on the front side of the trunk of a male subject. The antennas were tangentially polarized to the skin along the vertical direction, as in Fig. 1(b). The antennas were fixed 5 mm away from the skin to avoid a decrease of the antenna efficiency by the body coupling effects [3].

We used a multi-ports vector network analyzer (VNA) to measure the transmission S-parameters among the antennas as the channel measurements. The antennas and the VNA were connected through stable coaxial cables. The current influence from the cables was found ignorable to the measurements. The measurements were conducted in continuous wave (CW) mode over time at 2.45 GHz. Each measurement piece with fixed positions of the antennas contains 10 seconds observation at a sampling rate of 1 ms.

TABLE I
Setups and human body characterization of measurement campaign 1

Frequency	2.45 GHz	IF Bandwidth	10 kHz
Input power	0 dBm	Sweep mode	CW
Measurement length	10 s	Sampling rate	1 ms
Body height	183 cm	Body weight	80 Kg
Body trunk radius (ρ_{body})	14.5 cm	Arm radius (ρ_{arm})	4.2 cm
Arm-body spacing (d_{ab})	3 cm	Antenna height	122 cm

During the measurements, the subject was asked to stand on the ground and swing the arms to mimic the typical arm movement during walk. The arms swing in quasi-periodic way, which bring the dominant dynamic body-scattering effect to the investigated on-body channels.

The goal of this measurement campaign was to investigate different on-body channels by means of measurable geometry, i.e. a quantized geometric description of the channel distribution on the body. The statistics of the time-varying narrowband on-body fading can then be related with the channel geometry to enable a canonical characterization and modeling. In Fig. 2(a), the antennas were placed at the same height, forming horizontal on-body channels around the trunk. Each channel is then described explicitly by its Tx-Rx propagation distance measured on the trunk surface, and the relative position of the Tx to the trunk center. Fig. 2(b) describes the geometry quantization of the channels. Considering the channel distribution (front side of trunk) and the dominant body scattering (arm swing), the geometry of the body can be described by the radii of the arms (ρ_{arm}) and the trunk (ρ_{body}), and the space between the arms and the trunk (d_{ab}). The details of the measurement settings are listed in Table I.

B. Measurement setup 2

The measurement campaign from CEA-LETI was carried out in both anechoic chamber and indoor environments [12].

The test-bed was composed of a pulse step generator, a wideband real-time digital oscilloscope Tektronix TDS6124C, a power amplifier at Tx (about 35 dB in the band of interest), and several low-noise amplifiers at Rx (42 dB gain and noise figure of 2 dB), to obtain a distributed single-input-multiple-output (SIMO) configuration. The test-bed can simultaneously collect up to four channel impulse responses (CIRs) coming from different locations on the body. The CIRs were collected every 20 ms, each one enhanced by averaging 30 CIRs to improve the signal-to-noise ratio (SNR) of the measurements. Measurements were investigated in a large band, including 2.4 GHz and 3-5 GHz part of the UWB. In this paper, we focus only on the results at 2.4 GHz.

The employed antennas were compact 30 mm $\times$ 40 mm UWB antennas derived from [13], which were fixed at 5 mm away from the skin by dielectric foam blocks. Three different

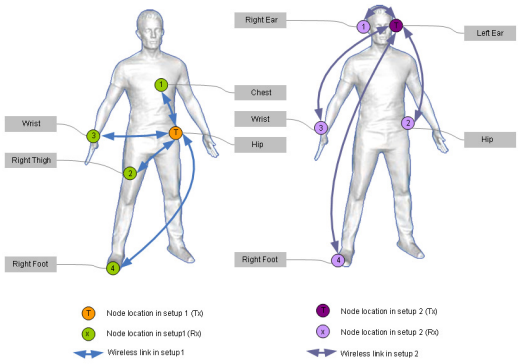

Fig. 3. Measured channels in setup 2: TX on Hip (left), TX on Ear (right) [12]

modes of body movements were investigated: standing *still*, *walking*, and *running* on a spot. Two sets of measurements were performed according to the antenna locations as depicted in Fig.3. In the first set, the Tx was on "Hip" (left side) and we collected simultaneously the received signals on "Chest", "Right Thigh", "Right Wrist" and "Right Foot". In the second set, the Tx was placed on "Left Ear" and we collected simultaneously the received signals on "Right Ear", "Hip", "Right Wrist" and "Right Foot". The variability of the human bodies was taken into account by repeating the measurements on 7 different subjects: heights from 1.69 m to 1.89 m, and weights from 58 kg to 79 kg. The non-homogeneity of the human body, and the variability of different subjects, suggest a scenario-based channel characterization and modeling, with respect to the locations of the antennas, the body movements, and the surrounding environment. The scenario-based approach identifies a specific *scenario* in measurement campaign 2 by:

- the $TX \in \{$Hip, Left Ear$\}$
- the $RX \in \{$Hip, Chest, Right Wrist, Right Thigh, Right Foot, Right Ear $\}$
- the movement $m \in \{$Still, Walking, Running$\}$
- the environment $e \in \{$Anechoic, Indoor$\}$

In brief, a particular *scenario* in measurement campaign 2 is noted as $\mathbb{S} = \{TX, RX, m, e\}$. The channel characterization and modeling are then specified to each scenario [14].

III. Fading Statistics and Modeling

The narrowband channel fading is the time-variation of the channel. The time-variation of on-body channels can be caused by the following reasons: the dynamic body scattering, the multipath (MPC) effects from the off-body scattering, and the modifications of the antenna properties during the body movements and the change of body postures. The issue of antenna de-embedding is not covered in this paper, yet it is important to obtain the correct physical on-body channels from the measurements.

The geometry-based measurement campaign 1 does not distinguish the fast fading and slow fading (shadowing) defined in conventional large-scale propagation, because there is no clear physical mechanism to strictly specify the two different fadings when only the dynamic body scattering is considered

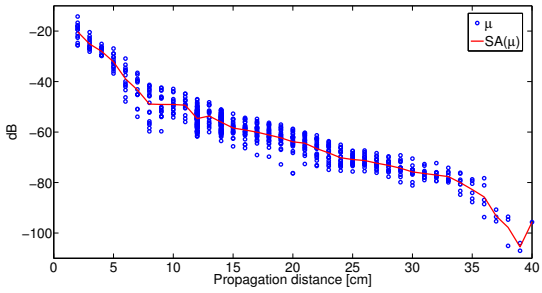

(a) Mean μ

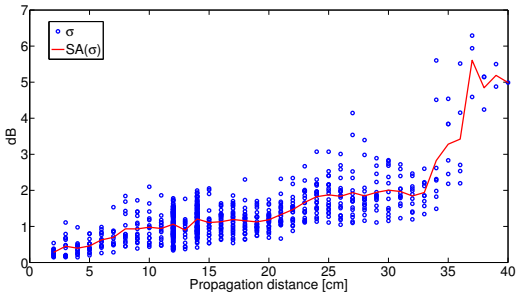

(b) STD σ

Fig. 4. Mean μ and STD σ of fading amplitude on a dB scale over the propagation distance, measurement campaign 1

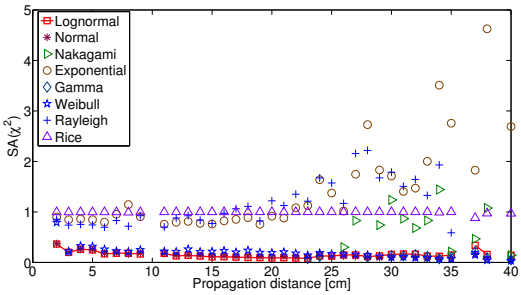

Fig. 5. $SA[\chi^2]$ comparison of various distribution estimations of the fading amplitude on a linear scale, measurement campaign 1

in the scenarios. The statistics of the horizontal on-body channels are then extracted from each measurement piece (10 s). In measurement campaign 1, the mean and standard deviation (std) of the channel fading amplitude are computed on dB scale, i.e. $\mu = E[|S_{xy}|_{dB}(t_n)]$ and $\sigma = STD[|S_{xy}|_{dB}(t_n)]$. Fig. 4 presents the measurement results of μ and σ, which are sorted by the propagation distance d_{xy} described in Fig. 2. In Fig. 4, each point at a given propagation distance represents a channel at a specific position. The different positions of the channels causes a spatial variation of μ and σ at each d_{xy}. The spatial average (SA) of μ and σ, i.e. the averaged values of μ and σ at each d_{xy}, are also plotted in Fig. 4, to describe the average trends of μ and σ along d_{xy}. The results show a linear decrease of μ, i.e. a path loss of 1.68 dB/cm for on-body propagation around the trunk in tangential z-polarization. A linear increase of σ at 0.09 dB/cm is observed when $d_{xy} < 30cm$, and a faster increase when d_{xy} is above 30 cm. The faster increase of σ of channels longer than 30

cm may due to an enhancement of non-line-of-sight (NLOS) propagation and a relatively increasing impact from the arm scattering to the channels.

The maximum likelihood estimator (MLE) is applied to compare the following distribution models of the fading amplitudes on linear scale in measurement campaign 1: Lognormal, Normal, Exponential, Weibull, Gamma, Nakagami, Rayleigh, and Rice. The Chi-square value, χ^2, is taken as the good-of-fitness test for the estimations.

For clarity, Fig. 5 compares the SA of χ^2 of different distribution estimations over the d_{xy} . It shows that within the range of the investigated propagation distances, the Lognormal distribution is among the best candidates to describe the distribution of fading amplitude on linear scale, i.e. normal distribution on dB scale. A similar conclusion can be found in [15] for static scenarios.

The scenario-based measurement campaign 2 distinguishes the shadowing/slow fading $\mathcal{S}(t_n)$ and the fast fading $\mathcal{F}(t_n)$ in the measured time-dependent power transfer function $\mathrm{P}(t_n)$ by the conventional definition:

$$\mathrm{P}(t_n) = \mathrm{G}_0 \cdot \mathcal{S}(t_n) \cdot \mathcal{F}(t_n), \tag{1}$$

where G_0 is the path loss based on each measurement piece. Examples of $\mathrm{P}(t_n)$ and $\mathrm{G}_0 \cdot \mathcal{S}(t_n)$ are demonstrated in Fig. 6, showing that the shadowing strictly depends on the movement mode. When the subject is in *still* scenarios, the slow varying component of $\mathrm{P}(t_n)$ is very small, since the shadowing condition of the body remains stationary.

The results from measurement campaign 2 show that the path loss on dB scale, $\mathrm{G}_0|_{dB}$, is a Gaussian random variable. The variance of $\mathrm{G}_0|_{dB}$ accounts for the dissimilarities among the human body investigated, and the local displacements of the antennas due to the different body shapes:

$$\mathrm{G}_0|_{dB} \sim \mathcal{N}(\mu_{0_{\mathbb{S}}}, \sigma_{0_{\mathbb{S}}}). \tag{2}$$

In Table II and Table III we resume the statistics of $\mathrm{G}_0|_{dB}$ for the investigated scenario respectively.

The std of $\mathrm{G}_0|_{dB}$, $\sigma_{0_{\mathbb{S}}}$, can be large especially in anechoic chamber, where the propagation occurs mainly by on-body creeping waves, LOS, and the ground reflection. On the other hand, the path loss of an identical on-body link in indoors is usually stronger than in anechoic chamber. This is because the propagation in indoors receives a significant amount of MPCs from the off-body environment, e.g. reflections of objects, which results in an extra energy contribution. This phenomenon is particularly evident when the Rx is shadowed by the body and the NLOS propagation occurs. For instance, in the Hip-Foot and Ear-Foot links we measured a channel gain up to 10 dB and 15 dB stronger in indoors than in anechoic chamber, as listed in Table II and Table III.

The statistical analysis on the shadowing is also carried out on dB scale, $\mathcal{S}(t_n)|_{dB}$, which follows a Normal distribution:

$$\mathcal{S}(t_n)|_{dB} \sim \mathcal{N}(0, \sigma_{s_{\mathbb{S}}}), \tag{3}$$

where $\sigma_{s_{\mathbb{S}}}$ describes the slow variation of $P(t_n)$ in each specific scenario $\mathbb{S}$. A summary on the $\sigma_{s_{\mathbb{S}}}$ is also presented in Table II and Table III.

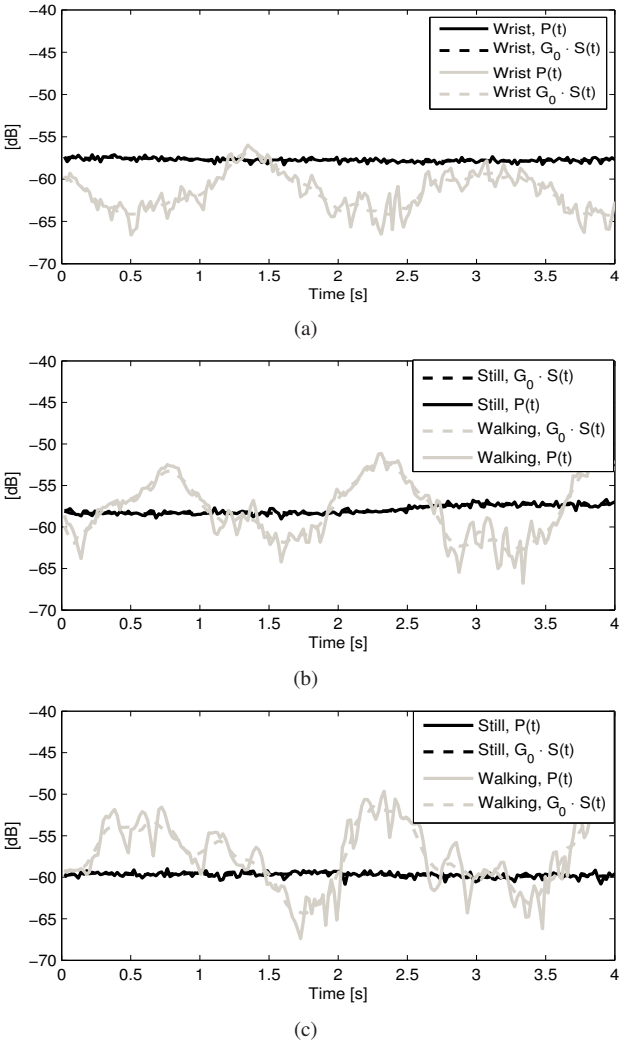

Fig. 6. Time-variant power transfer function and slow fading in indoor in measurement campaign 2: Hip-to-Wrist (a), Hip-to-Thigh(b),Hip-to-Foot(c)

As expected, we found a large $\sigma_{s_{\mathbb{S}}}$ on moving bodies, especially in the *walking* scenarios. The $\sigma_{s_{\mathbb{S}}}$ in a *running on a spot* scenario is usually smaller than in a *walking* scenario, because of the particular running mode. When the subject is running on a spot, his legs move faster but oscillate less than in walking cases. And the arms will also be close to the body, limiting their range of oscillation. Consequently, these cause a smaller $\sigma_{s_{\mathbb{S}}}$. We also observe that the slow fading is generally smaller in indoors, because the extra reflections from the off-body environment mitigate the shadowing effect of the body.

The fast fading component is expressed as $\mathcal{F}(t_n) = |\eta(t_n)|^2$. Measurement results show that $|\eta(t_n)|$ follows a Rice distribution. High K-factors ($K = \nu_\chi^2/2\sigma_\chi^2$) are observed in the *still* scenarios, which indicates a main path with a strong energy concentration and no significant body movements besides the breathing. On the contrary, in walking scenarios, the body movements enhance the fast fading, hence the K-factor drops. A typical example can be found in the Hip-Foot link in Fig. 7, where the nodes are often in NLOS and the propagation relies on the reflections and diffractions of the body. In this case, the K-factors drop close to 0, turning the fast fading

TABLE II
TX ON HIP: CHANNEL GAIN AND SHADOWING PARAMETERS IN DB, MEASUREMENT CAMPAIGN 2

	RX on	Anechoic Chamber			Indoor		
		μ_{0_S}	σ_{0_S}	σ_{S_S}	μ_{0_S}	σ_{0_S}	σ_{S_S}
Still	Chest	-60.88	4.15	0.61	-54.65	4.81	0.60
	Thigh	-64.31	1.54	0.41	-60.71	2.62	0.24
	R Wrist	-63.21	2.61	0.95	-57.86	5.10	0.26
	R Foot	-67.12	5.18	0.41	-60.44	2.26	0.24
Walking	Chest	-53.37	7.86	2.15	-51.75	7.27	1.52
	Thigh	-61.97	6.49	5.27	-59.48	3.04	3.27
	R Wrist	-62.17	5.96	4.31	-59.59	4.20	2.66
	R Foot	-68.60	7.41	4.97	-58.33	2.59	2.57
Running	Chest	-52.78	3.34	2.39	-47.94	7.54	2.00
	Thigh	-59.12	4.43	2.47	-57.84	3.52	1.98
	R Wrist	-65.86	4.31	3.49	-61.78	3.89	2.37
	R Foot	-71.22	8.43	2.69	-60.47	1.96	1.80

TABLE III
TX ON LEFT EAR: CHANNEL GAIN AND SHADOWING PARAMETERS IN DB, MEASUREMENT CAMPAIGN 2

	RX on	Anechoic Chamber			Indoor		
		μ_{0_S}	σ_{0_S}	σ_{S_S}	μ_{0_S}	σ_{0_S}	σ_{S_S}
Still	R. Ear	-63.25	6.35	0.23	-60.22	3.15	0.21
	Hip	-60.13	8.94	0.45	-60.28	6.07	0.28
	R. Wrist	-72.9	2.63	1.15	-64.47	3.28	0.31
	R. Foot	-75.35	4.53	0.56	-62.72	2.19	0.3
Walking	R. Ear	-61.00	2.7	0.54	-60.03	3.08	0.9
	Hip	-57.93	7.17	2.07	-58.77	4.94	2.2
	R. Wrist	-71.85	2.91	3.35	-63.04	1.98	1.8
	R. Foot	-72.99	4.65	4.21	-61.00	1.31	2.02
Running	R. Ear	-61.36	3.64	0.52	-60.74	5.3	0.7
	Hip	-63.83	7.54	2.82	-60.76	5.7	2.19
	R. Wrist	-71.99	2.22	2.98	-63.56	2.23	1.88
	R. Foot	-77.7	3.42	1.57	-62.70	1.15	1.24

distribution into a Rayleigh distribution.

The off-body scattering effect and the increasing number of MPCs in indoors also enhance the fast fading. These effects are directly transposed on the statistics of $|\eta(t_n)|$ and the K factors. In Fig. 7 we compare the K factor of the fast fading distribution in indoors and in anechoic chamber. It shows that the K factor in indoors is sensibly lower than in anechoic chamber, which describes a more important contribution from the NLOS propagation components.

IV. DOPPLER DISPERSION

The Doppler spectra were investigated and modeled in measurement campaign 2 in [16]. Fig. 8 presents the normalized Doppler spectra in *walking* scenarios in anechoic chamber. When one node is on the trunk and the other one is on a moving limb, the Tx-Rx distance changes slightly during the body movements. However, the relative velocity of the Rx to the Tx is low, and the time-variance of the Tx-Rx distance is mainly given by the varying postures of the body. Consequently the Doppler spectrum is still centered at $f_\nu = 0$,

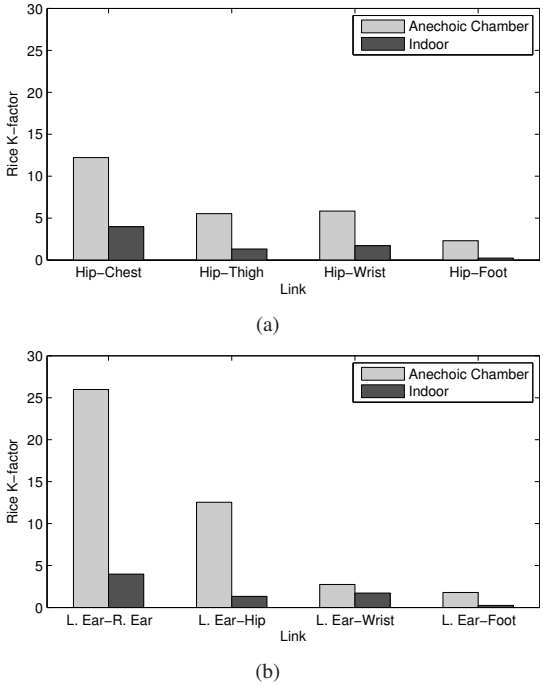

Fig. 7. K factor in Walking scenarios, measurement campaign 2: TX on hip (a) and on the left ear (b)

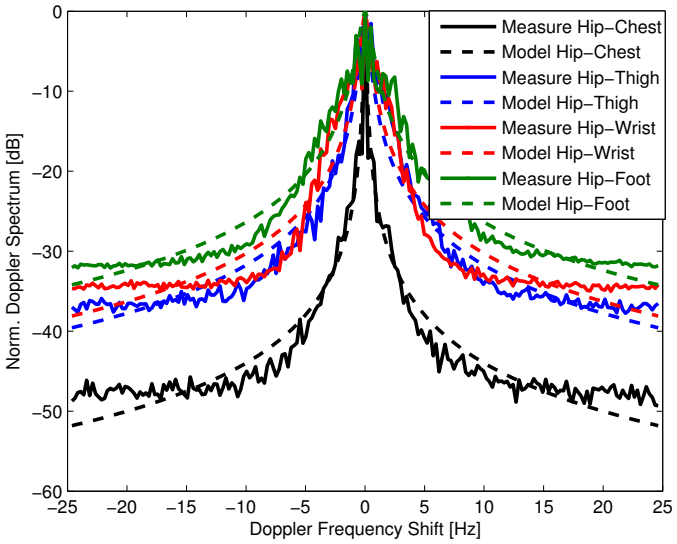

Fig. 8. Normalized Doppler Spectra: human walking in anechoic chamber, measurement campaign 2

f_ν as the Doppler frequency shift, but presenting a smoother behavior, as shown in Fig. 8.

The difference on the floor levels of the Doppler spectra in Fig. 8, when the Rx is on the chest, and when the Rx is on the limbs, can be explained by the increased freedom of mobility in the latter case. Given this behavior it is useful to identify the Doppler bandwidths by a threshold, e.g. -20 dB below the peak value at f_ν=0 Hz, instead of the maximum Doppler shift. In Table IV, the results of the Doppler bandwidth in anechoic chamber are listed.

A rigorous mathematical formulation of Doppler spectrum from moving scatterers has been recently given in [17]. By

TABLE IV
BANDWIDTH AT -20 dB AND MODEL PARAMETERS OF ON-BODY DOPPLER SPECTRUM IN ANECHOIC CHAMBER, MEASUREMENT CAMPAIGN 2

Radio link	BW_{-20dB}[Hz]	γ
Hip-Chest	1.5	0.004
Hip-Thigh	6.4	0.067
Hip-Wrist	7.3	0.094
Hip-Foot	10	0.231
L. Ear-R. Ear	0.3	0.013
L. Ear-Hip	1.3	0.007
L. Ear-Wrist	8	0.574
L. Ear-Foot	12.6	0.862

assuming uniform scattering pattern and independence of scatterers, the Doppler spectrum can be decomposed by Bessel and Legendre functions [17]. Instead of Laplacian distribution a simplified expression of the normalized Doppler spectrum can be the following:

$$D(\nu)_{On-Body} = \frac{1}{\gamma + \nu^2} \tag{4}$$

Fig. 8 shows a good approximation of this model with the measurement results, by using the values of γ listed in Tab.IV. A small value of γ represents a modest degree of mobility, e.g. in the Hip-Chest, Ear-Ear and Ear-Hip links.

V. FADING CORRELATION PROPERTIES

The dynamic body scattering causes a deep fading of on-body channels in time and spatial domains. It brings to a large fluctuation of the SNR in realistic WBAN links, which restricts the performance of a power-limited long-term on-body communication. Cooperative techniques, as studied in [18], [19], are found effective to mitigate such fading effects by exploiting the channel spatial diversity. In the design of cooperative protocols in WBANs, the spatial correlation of the on-body channel fading is a fundamental parameter to evaluate the cooperation performance.

The work in measurement campaign 1 investigated the correlation between the channel S_{21} and S_{31} as described in Fig. 2(b) [3]. The correlation coefficient, $\rho_{21,31}(d_{23})$, is computed by the fading amplitudes on dB scale, since the channels were found to be lognormally distributed in Fig. 5.

$$\rho_{21,31} = \frac{E[(|S_{21}|_{dB} - \mu_{|S_{21}|_{dB}})(|S_{31}|_{dB} - \mu_{|S_{31}|_{dB}})]}{\sigma_{|S_{21}|_{dB}}\sigma_{|S_{31}|_{dB}}}, \tag{5}$$

From geometric point of view, S_{21} and S_{31} are overlapping channels sharing a common Tx (antenna 1) and differ in the distance between antennas 2 and 3 (d_{23}). d_{23} is supposed to bring a de-correlation effect between the channels. The increase of d_{23} is therefore expected to lower the correlation between S_{21} and S_{31}. Naturally, a boundary condition $\rho_{21,31}(d_{23}) = 1$, when $d_{23} = 0$, should hold, representing the complete overlapping of S_{21} and S_{31}.

Two collections of measurement results, given $d_{12} = 12$ cm and $d_{12} = 14$ cm, are presented in Fig. 9. The results show a decreasing trend of $\rho_{21,31}$ as d_{23} increases. It validates our assumption on the de-correlation effect of d_{23}. From the

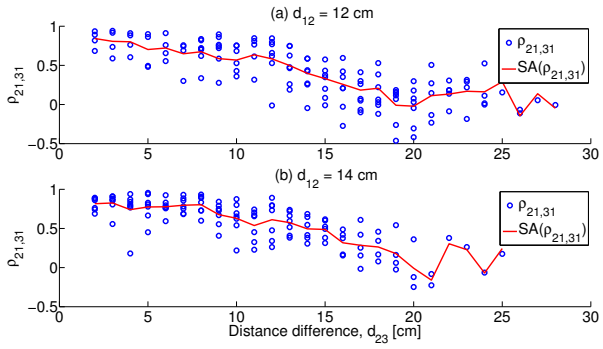

Fig. 9. Collections of $\rho_{21,31}$ at different d_{12} obtained from measurement campaign 1

averaged value, $SA[\rho_{21,31}]$, it was found that the average de-correlation distance of d_{23} ($\rho_{21,31} \leqslant 0.7$) varies between 6 cm and 10 cm.

Based on Fig. 9, an experimental model for $\rho_{21,31}$ as a linear function of d_{23} (cm) in (6) is proposed,

$$\rho_{21,31} = \begin{cases} 1 - 0.043 d_{23} & 0 \leqslant d_{23} < 23 \\ 0 & d_{23} \geqslant 23 \end{cases} \tag{6}$$

The work in measurement campaign 2 investigates the shadowing correlation coefficients in scenarios where the Tx was on the Hip, in both anechoic chamber and indoor environment. Fig. 10 presents the results in different link distributions. It shows that the shadowing correlation in anechoic chamber is only slightly higher than in indoors. This shows that in both anechoic chamber and indoor environment, the dynamic body scattering is the main source to produce the shadowing to the on-body propagation. Moreover, the shadowing correlation is relatively high when the body is static, probably due to the statistical error in the time-limited channel observation. Nevertheless, the small value of σ_{s_S} reduces the correlation significance in *still* scenarios. The results also show a coincidence of achieving the highest fading correlation in the scenarios containing high shadowing (generally, when one antenna is on a limb), as in the Hip-Wrist, Hip-high and Hip-Foot links in the walking scenarios in Fig. 10.

It is interesting to observe a negative shadowing correlation in Wrist/Thigh and Wrist/Foot links in Fig. 10. This is because that the Rxs are all on the right limbs while the Tx is on the left side. During a walk the subjects tend to alternate the movements of legs and arms, which consequently causes the time-variation of the shadowing on right wrist opposite to it on the right thigh and right foot, and therefore a high negative correlation between the links. This macro effect is verified in both anechoic and indoor environments.

VI. ANALYTICAL MODELING

The analytical model is an extension from earlier work in [20]. The modeling principle is to simplify the shapes of different body components, such as the trunk, arms, and legs, as infinite cylinders, so that the fields of line source or point source with the body scattering can be solved in close form. To ensure the accuracy of the model with such geometry, the

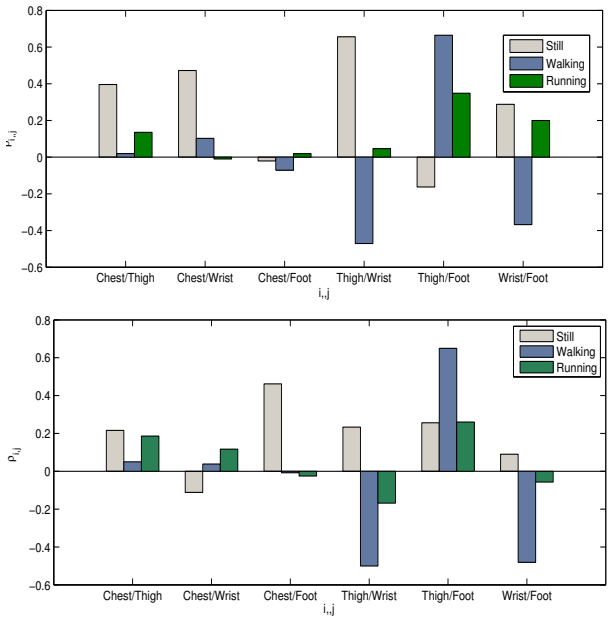

Fig. 10. Shadowing correlation in measurement campaign 2, Tx placed on the Hip: anechoic chamber (up), indoor (down)

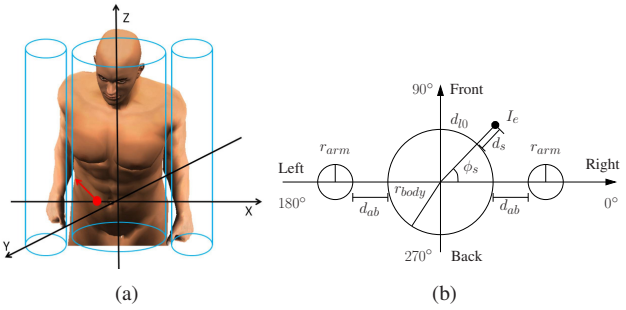

Fig. 11. (a) Geometric modeling of the body and the source, (b) Geometric description of the body and the source in azimuth plane. r_{body} is the trunk radius, r_{arm} is the arm radius, d_{ab} is the distance between the arm and the trunk, and d_s is the distance from the source to the trunk surface; $d_{l0} = (r_{body} + d_s)\phi_s$ is the corresponding distance around the body.

investigated on-body channels have to be away from the edges of the body, e.g. the shoulders and the hands. With respect to measurement campaign 1, three infinite, homogeneous, and lossy cylinders are applied to model the trunk and the arms of the body, as in Fig. 11(a). The assumption of homogeneous cylinders is based on the observation of rapid power decay when radio waves penetrate the body. All the cylinders are vertically placed and are allowed to have parallel movements in the horizontal plane. The size and the initial positions of the body can be referred in Table. I. The conductivity of the cylinders is determined by the cole-cole model [21], which are assumed to be composed by dry skin with respect to the measurements.

The Tx antenna is simplified into a polarized point source with constant current intensity. The direction of the polarization of Tx is described in the global z-polar coordinate, i.e. the source current is decomposed into polarization components along the z (tangential polarization along the vertical direction), ϕ (tangential polarization along the horizontal direction), and ρ (normal polarization to the skin) directions. For computation simplicity, the Tx is fixed at horizontal plane $z = 0$, so the fields are symmetric along the z direction. The Rx antenna is also simplified into a point with its polarization also described in the z-polar coordinate in the same way.

The positions of the cylinders and the Tx in azimuth plane can be described in the global z-polar coordinate, as in Fig. 11(b).

The desired on-body channel, given the positions of the Tx and Rx, is obtained by solving the full-wave fields of the point source with multiple cylinder scattering. The field solution contains two steps. First, by [20], the field of the point source is transferred into the integration of line source fields with different wave-numbers along z and ρ directions as:

$$E^{point}(\rho, \phi, z) = \frac{1}{2\pi} \int_{-\infty}^{-\infty} E^{line}(\rho, \phi)(k_z) e^{-jk_z z} dk_z, \quad (7)$$

where k_z is the wave-number along the z direction. The singularity problem in the integration is also well described in [20].

Secondly, for each line source, the multiple cylinder scattering is solved by applying the addition theorem by [22] to explicit the interacting processes of the scattered fields from different cylinders. In general, the field solution is an iterative process described by the boundary condition, which can be understood as that the scattered fields of each cylinder excited by the initial incident field from the source will re-excite higher order scattered fields when they reached the surfaces of the other cylinders, as described as:

$$E_1^{s,p} = E^{i,p} + E_2^{s,p} + \sum_{q \neq p}^{P} E^{s,q}, \quad (8)$$

where $E_1^{s,p}$ and $E_2^{s,p}$ stand for the scattered fields from cylinder p inside and outside the surface of cylinder p, $E^{i,p}$ stands for the incident field from the polarized source at the surface of cylinder p, and $E^{s,q}$ stands for the scattered fields from the other cylinders arriving at the surface of cylinder p. The complete full-wave field solution of each polarization component (z, ρ, ϕ) is well described in [23]. An efficient algorithm for a numerical approximation can be found in [24], [25]. The model provides a general field solution with arbitrary polarization of the Tx and Rx.

When the on-body channel is distributed on the horizontal plane and both the Tx and Rx are in z-polarization, a simplified field solution can be realized by considering the field solution of a z-polarized line source with multiple cylinder scattering. A simulation example is shown in Fig. 12 to compare the effect of the joint arm-trunk scattering to the trunk scattering in the azimuth plane. The shadowing effect at the back of the trunk, and the interference from the arm scattering are clearly observed.

The dynamic body scattering is modeled by extending the above static field solution into a series of time-consecutive scenarios with different positions of the arms at the azimuth

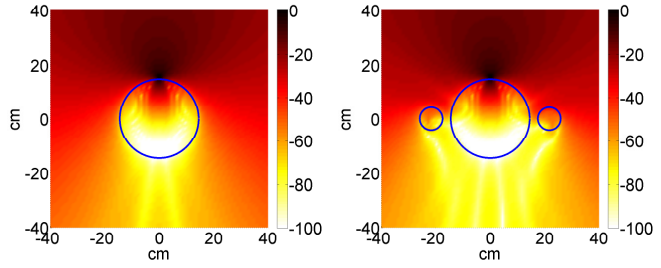

(a) (b)

Fig. 12. Simulated normalized field of a vertical polarized source and scattering by single cylinder (a) and by multiple cylinders (b) ; the source is placed on the trunk center $\phi_s = 90°$, 0.5 cm away from the trunk surface

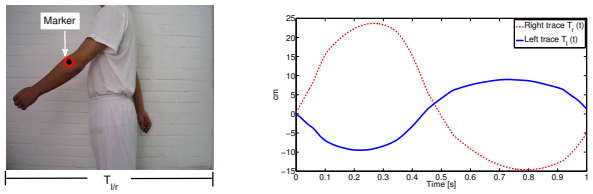

(a) (b)

Fig. 13. The arm swing modeling, (a) depicts the tracing of arm swinging through a black marker on the arms, (b) presents the normalized trace functions of the arms over one cycle

plane, as a result of the arm swing investigated in measurement campaign 1. The arm swing is modeled as periodic traces along y direction in Fig. 11(b). In practice, the traces are recorded from realistic arm-swing motion as in Fig. 13(a). The samples of the traces are shown in Fig. 13(b).

The model is evaluated by comparing with measurement campaign 1 on the deterministic and stochastic properties of the dynamic on-body channels. Simulations repeat the scenarios in the measurements described in Fig. 2 and in Table I, where the statistics of the simulated channels are extracted in the same way. Fig. 14 first presents a deterministic comparison on the fading amplitude over one cycle between a measurement sample and the corresponding simulation. In the comparison, the local peaks between the measurement and the simulation result are well matched, and a small mean square error (MSE) of 1.21 dB is achieved. The symmetric waveforms in the first and second half cycle of the simulation result is also consistent with the regular arm swing.

The channel statistics, μ, σ, and $\rho_{21,31}$, as investigated in the measurements in Fig. 4 and Fig. 9, are compared to those obtained from the simulations in Fig. 15. The statistical similarity on the path loss, the fading variation, and the channel fading spatial correlation in the comparison validates the model performance in the considered scenarios.

This model provides a generalized field solution of multiple cylinder scattering, which can also be applied to other scenarios where the body scattering can be approximated by parallel cylinder scattering. The performance of the model is restricted by the infinite cylinder approximation and the small-scale body movements so that the parallel motion assumption holds true. It also requires that the size of the antennas should

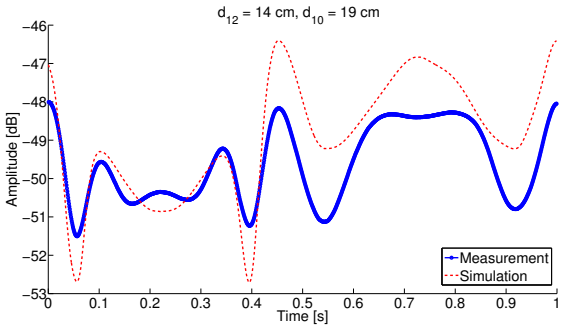

Fig. 14. Deterministic comparison of the channel fading amplitude (dB) in one cycle with one measurement sample of S_{21} in measurement campaign 1 ($d_{12} = 14cm$, $d_{10} = 19cm$)

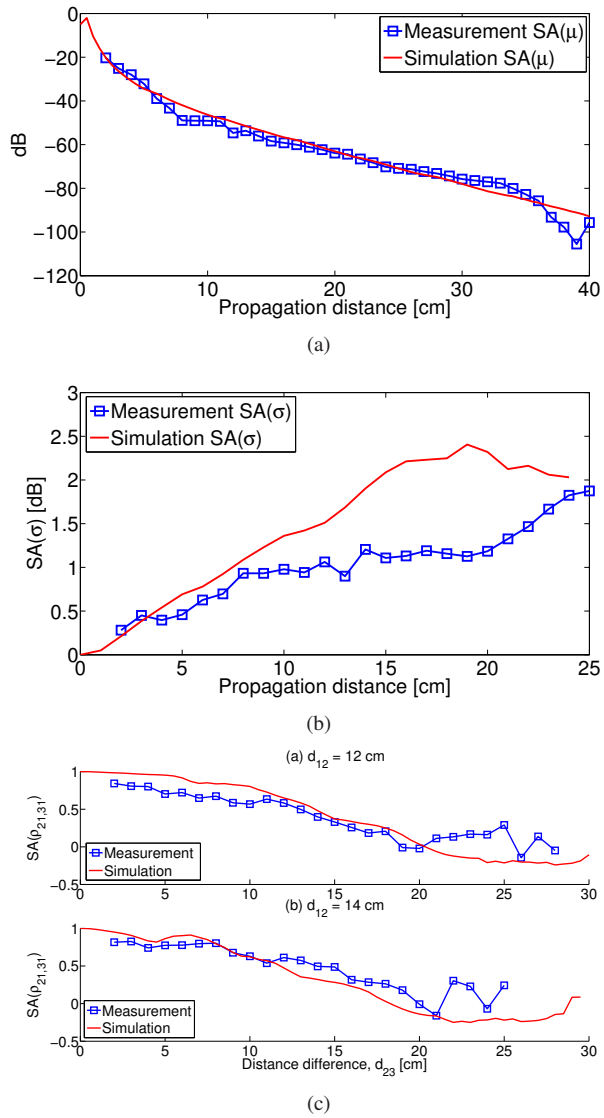

(a) (b) (c)

Fig. 15. Statistical comparison between the simulations and measurement campaign 1 on the (a) averaged mean, (b) std, and (c) correlation coefficient $\rho_{21,31}$ of the on-body channels fading amplitude on dB scale

be small enough that the current distribution on the antennas will not bring large mismatch when approximated by a point source.

VII. Conclusion

We have presented an overview of some results on the on-body dynamic channel modeling activity obtained during the COST 2100 action. The works from CEA-LETI and UCL-ULB have been focusing on the time-variant aspects of the on-body channel, attempting to cover those issues that have not been addressed in the previous models. The adopted approaches present some discrepancies for what concerns the way the measurements were performed and analyzed. Nevertheless, the obtained results have some complementarity, in terms of scenarios investigated and implemented models, representing a step forward in the dynamic on-body channel modeling. Among these, the existence of a long term, a medium and a short term in on-body channel fading has been pointed out and statistically modeled. In both measurement campaigns, it has been shown that body shadowing is the predominant effect to the time-variation of on-body channels, and its correlation properties strongly depend on the considered scenario. Moreover, the simulation results, obtained by a cylindrical scatterer representation of the human body, show good consistency with measurements.

The achievements in the COST 2100 action have also pointed out the absence of sufficient investigation on some important issues like de-embedding antenna from the channel, polarization sensitivity, space-time correlation over different bands, and delay-doppler spectrum in WBAN channel modeling, which are necessary to draw a complete image of on-body radio propagation, and serve as fundamental knowledge for the design of energy-efficient and cooperative on-body wireless communication systems.

Acknowledgments

This work has been supported by the ANR French project BANET, the European Commission under the FP7 project WiserBAN , and the Walloon Region under the WIST2 project WALIBI.

References

[1] J. Ryckaert, P. De Doncker, R. Meys, A. de Le Hoye, and S. Donnay, "Channel model for wireless communication around human body," *Electronics Letters*, vol. 40, no. 9, pp. 543 – 544, april 2004.

[2] R. D'Errico and L. Ouvry, "Time-variant ban channel characterization," in *Proc. IEEE 20th Int. Symp. on PIMRC*, sep. 2009, pp. 3000 –3004.

[3] L. Liu, P. De Doncker, and C. Oestges, "Fading correlation measurement and modeling on the front side of a human body," in *Proc. of 3rd EuCAP*, march 2009, pp. 969 –973.

[4] S. van Roy, C. Oestges, F. Horlin, and P. De Doncker, "A comprehensive channel model for uwb multisensor multiantenna body area networks," *IEEE Trans. on Antennas and Propagation,*, vol. 58, no. 1, pp. 163 –170, jan. 2010.

[5] E. Monton, J. Hernandez, J. Blasco, T. Herve, J. Micallef, I. Grech, A. Brincat, and V. Traver, "Body area network for wireless patient monitoring," *IET Communications*, vol. 2, no. 2, pp. 215 –222, feb. 2008.

[6] Y. Zhao, Y. Hao, A. Alomainy, and C. Parini, "Uwb on-body radio channel modeling using ray theory and subband fdtd method," *IEEE Trans. on Microwave Theory and Techniques,*, vol. 54, no. 4, pp. 1827 – 1835, jun. 2006.

[7] D. Miniutti, L. Hanlen, D. Smith, A. Zhang, D. Lewis, D. Rodda, and B. Gilbert, "Narrowband Channel Characterization for Body Area Networks," IEEE P802.15-08-0421-00-0006, July 2008.

[8] K. Y. Yazdandoost and K. Sayrafian-Pour, "Channel Model for Body Area Network (BAN)," IEEE P802.15-08-0780-09-0006, April, 2009.

[9] S. Cotton, G. Conway, and W. Scanlon, "A Time-Domain Approach to the Analysis and Modeling of On-Body Propagation Characteristics Using Synchronized Measurements at 2.45 GHz," *IEEE Trans. on Antennas and Propagation*, vol. 57, no. 4, pp. 943–955, 2009.

[10] B. Zhen, M. Kim, J.-I. Takada, and R. Kohno, "Characterization and modeling of dynamic on-body propagation at 4.5 ghz," *IEEE Antennas and Wireless Propagation Letters,*, vol. 8, pp. 1263 –1267, 2009.

[11] "COST Action 2100 - Pervasive Mobile & Ambient Wireless Communications," http://www.cost2100.org/.

[12] R. D'Errico and L. Ouvry, "Time-variant BAN Channel Characterization," in *Proc. of IEEE 20th International Symposium on Personal, Indoor and Mobile Radio Communications (PIMRC 2009)*, Tokyo, Japan, Sept. 2009, pp. 3000 –3004.

[13] Demeestere, F. and Delaveaud, C. and Keignart, J., "A compact UWB antenna with a wide band circuit model and a time domain characterization," in *Proc. of the 2006 IEEE International Conference on Ultra-Wideband (ICUWB 2006)*, Waltham, MA, USA, 2006, pp. 345–350.

[14] R. DErrico and L. Ouvry, "A Statistical Model for On-Body Dynamic Channels," *International Journal of Wireless Information Networks*, pp. 1–13.

[15] A. F. Molisch, D. Cassioli, C. Chong, et al., "A comprehensive standarization model for ultrawideband propagation channels," *IEEE Trans. on Antennas and Propagation*, vol. 54, no. 11, pp. 3154–3166, November 2006.

[16] R. D'Errico and L. Ouvry, "Doppler characteristics and correlation proprieties of on-body channels," in *Proc. of 5th EUCAP*, april 2011, pp. 2977 –2981.

[17] J. Andersen, J. Nielsen, G. Pedersen, G. Bauch, and G. Dietl, "Doppler spectrum from moving scatterers in a random environment," *IEEE Trans. on Wireless Communications*, vol. 8, no. 6, pp. 3270–3277, 2009.

[18] J. Gorce, C. Goursaud, G. Villemeaud, R. D'Errico, and L. Ouvry, "Opportunistic relaying protocols for human monitoring in BANs," in *Proc. of IEEE 20th International Symposium on Personal, Indoor and Mobile Radio Communications (PIMRC 2009)*, Tokyo, Japan, Sept. 2009, pp. 732 – 736.

[19] Y. Chen, J. Teo, J. Lai, E. Gunawan, K. S. Low, C. B. Soh, and P. Rapajic, "Cooperative communications in ultra-wideband wireless body area networks: Channel modeling and system diversity analysis," *IEEE Journal on Selected Areas in Communications,*, vol. 27, no. 1, pp. 5 –16, january 2009.

[20] A. Fort, G. Roqueta, C. Craeye, and C. Oestges, "A body area propagation model derived from fundamental principles: Analytical analysis and comparison with measurement," *IEEE Trans. on AP*, vol. 58, no. 2, February 2010.

[21] P. S. Hall and Y. Hao, *Antennas and propagation for body-centric wireless communications*. Artec House,London, 2006.

[22] M. Abramowitz, I. A. Stegun, and P. M. Morse, *Handbook of mathematical functions*. GPO, 1964.

[23] L. Liu, F. Keshmiri, C. Craeye, P. De Doncker, and C. Oestges, "An analytical modeling of polarized time-variant on-body propagation channels with dynamic body scattering," *EURASIP Journal on Wireless Communications and Networking,*, vol. 2011, apr. 2011.

[24] F. Keshmiri and C. Craeye, "Wave propagation from sources with arbitrary polarization next to the human body," in *Proc. of 2010 IEEE Antennas and Propagation Society International Symposium (APSURSI),*, july 2010.

[25] L. Liu, F. Keshmiri, P. De Doncker, C. Craeye, and C. Oestges, "3-d body scattering interference to vertically polarized on-body propagation," in *Proc. of 2010 IEEE Antennas and Propagation Society International Symposium (APSURSI),*, july 2010, pp. 1 –4.

Lingfeng Liu was born in Jiujiang, Jiangxi, China, on Oct. 25, 1983. He received the B.S. degree in Electronic Information Engineering from Wuhan University, China, in 2005 and the M.S. degree in Signal and Information Processing in Communications from Aalborg University, Denmark, in 2007. Since 2007, he has been working as a research assistant in the ICTEAM Electrical Engineering department of Université catholique de Louvain (UCL), Belgium. He is also a PhD student in the ICTEAM department of UCL and in the OPERA department of Université libre de Bruxelles (ULB), Belgium. His research interests during the PhD study cover the channel characterization and modeling in body area networks (BAN), MIMO channel modeling and estimation, and design of cooperative communication networks. Since 2008, he has been an active member of the COST 2100 action and the NEWCOM++ action. He is also a member of the COST IC1004 action.

Raffaele D'Errico received the Laurea degree in Telecommunications Engineering from the University of Bologna, Italy, in 2005, and the PhD degree in from University of Orsay (Paris XI, France) and University of Bologna, in 2008. He received two Best Paper Awards, as first author from the IEEE Personal, Indoor and Mobile Radio Communications Symposium 2009, for his article "Time-variant BAN Channel Characterization" and, as co-author from the IFIP International Conference on New Technologies, Mobility and Security 2011, for the article "Topology Dynamics and Network Architecture Performance in Wireless Body Sensor Networks". Since 2007 he has been also actively participating to COST 2100 activities, focusing more specifically on channel modeling in Wireless Body Area Networks. Since 2009 he is with the Laboratory of Electronic and Information Technologies of the French Atomic Energy Commission (CEA-LETI). His more general research interests concern channel modeling for wireless sensor networks, UWB single/multiple antennas and antennas for Body Area Networks.

Laurent Ouvry received the diploma of French "Grande Ecole" SUPELEC in 1994 and M.S. degree of Rennes University in 1995 with a speciality in RF, antennas and digital signal processing and communications. He joined CEA-Leti in 1997, where he took the lead of the digital communication lab in 2001. Since 2004, he has been responsible for impulse radio UWB low data rate projects at CEA-Leti and initiated system activities on ultra low power for IEEE802.15.4 compliant radios. He was involved in the key ICT IP projects on UWB and has been an active contributor to the IEEE802.15.4a UWB standard definition. He is also involved in key ICT IP projects related to wireless sensor networks. Since 2007, he is working in the area of Body Area Networks and is involved in the IEE802.15.6 standardization for BANs.

Philippe De Doncker was born in Brussels, Belgium, in 1973. He received the M.Sc. degree in Physics Engineering from the Universit libre de Bruxelles in 1996, and the PhD degree from the same University in 2001. He is now Professor with the Wireless Communications Group of the OPERA Department at the Universit libre de Bruxelles. His research interest focus on electromagnetics and channel modeling for wireless communications.

Claude Oestges received the M.Sc. and Ph.D. degrees in Electrical Engineering from the Universit catholique de Louvain (UCL), Louvain-la-Neuve, Belgium, respectively in 1996 and 2000. In January 2001, he joined as a post-doctoral scholar the Smart Antennas Research Group (Information Systems Laboratory), Stanford University, CA, USA. From January 2002 to September 2005, he was associated with the Microwave Laboratory UCL as a post-doctoral fellow of the Belgian Fonds de la Recherche Scientifique (FRS). Claude Oestges is presently a FRS Research Associate and Assistant Professor with the Electrical Engineering Department, Institute for Information and Communication Technologies, Electronics and Applied Mathematics, UCL. He is the author or co-author of two books and more than 150 journal papers and conference communications, and was the recipient of the 1999-2000 IET Marconi Premium Award and of the 2004 IEEE Vehicular Technology Society Neal Shepherd Award.